ADVANCED ENERGY MATERIALS
www.advenergymat.de

Solvent-Mediated Formation of Quasi-2D Dion-Jacobson Phases on 3D Perovskites for Inverted Solar Cells Over 23% Efficiency

*Shripathi Ramakrishnan, Donghoon Song, Yuanze Xu, Xiaoyu Zhang, Gavin Aksoy, Mircea Cotlet, Mingxing Li, Yugang Zhang, and Qiuming Yu**

2D-on-3D (2D/3D) perovskite heterostructures present a promising strategy to realize efficient and stable photovoltaics. However, their applicability in inverted solar cells is limited due to the quantum confinement of the 2D-layer and solvent incompatibilities that disrupt the underlying 3D layer, hampering electron transport at the 2D/3D interface. Herein, solvent-dependent formation dynamics and structural evolution of 2D/3D heterostructures are investigated via in situ X-ray scattering. It is revealed that solvent interaction with the 3D surface determines the formation sequence and spatial distribution of quasi-2D phases with $n = 2$–4. Isopropanol (IPA) reconstructs the perovskite into a PbI_2-rich surface, forming a strata with smaller n first, followed by a thinner substratum of larger n. In contrast, 2,2,2-Trifluoroethanol (TFE) preserves the 3D surface, promoting the formation of uniformly distributed larger n domains first, and smaller n last. Leveraging these insights, Dion–Jacobson perovskites are used with superior charge transport properties and structural robustness to fabricate 2D/3D heterostructures dominated by $n \geq 3$ and engineer a favorable energy landscape for electron tunneling. Inverted solar cells based on 3-Aminomethylpyridine and TFE achieve a champion efficiency of 23.60%, with V_{oc} and FF of 1.19 V and 84.5%, respectively, and superior stabilities with t_{94} of 960 h under thermal stress.

1. Introduction

2D metal-halide perovskites (2D-MHPs) have emerged as a new family of photovoltaic materials proven to resolve the extrinsic stability in perovskites.[1,2] Typically, 2D-MHP frameworks are composed of n layers of corner-sharing $[BX_6]^{4-}$ octahedral frameworks sandwiched between two layers of bulky organic ligands.[3,4] Among these, two prominent 2D-MHP classes observed and characterized include the Ruddlesden-Popper perovskite (RPP) phase $A'_2(A)_{n-1}B_nX_{3n+1}$ and the Dion–Jacobson perovskite (DJP) phase $A''(A)_{n-1}B_nX_{3n+1}$, where A' and A'' are bulky organic mono- and diammonium ligands, respectively.[5] However, the coexistence of high efficiency and long-term stability has become a crucial requirement for the application of perovskite solar cells (PSCs). While 2D-MHP films with $n \geq 4$ exhibit excellent operational stabilities,[6–8] the power conversion efficiencies (PCEs) of the resulting devices significantly fall behind their 3D counterparts (3D-MHPs).[9–11]

To date, the most promising strategy to leverage the structural integrity of 2D-MHPs with the superior carrier dynamics of 3D-MHPs involves the formation of 2D-on-3D (2D/3D) heterostructures.[12,13] Typically, a layer of ligand salts is deposited atop a 3D-MHP, leading to the formation of $n = 1$ or 2 2D-MHP phases on the 3D-MHP surface, passivating surface traps and facilitating electron-blocking,[14] significantly improving the open-circuit voltage V_{oc} and fill factor FF of arising solar cells.[15] However, this strategy has invoked mixed results for the commercially relevant positive-intrinsic-negative p–i–n structured PSCs, where photogenerated electrons and holes in perovskites are collected by the top metal cathode and the bottom transparent conductive oxide anode, respectively.[16] The quantum-confinement effect imposed by the bulky ligands leads to shallower conduction band minima in 2D-MHPs compared to 3D-MHPs. As a result, the arising 2D/3D heterostructures exhibit electron blocking, which is detrimental to electron collection in p–i–n PSCs. Gharibzadeh et al. reported the use of phenylethylammonium chloride (PEACl) for dual passivation of grain boundaries and perovskite surface to form mixed domains of $n = 1$ and 2 RPP phases to achieve a high V_{oc} of 1.16 V on p–i–n PSCs.[17] More recently, Huang et al. regulated the rate of cation exchange during 2D/3D heterostructure formation via a diamine masking reagent on a 3D-MHP surface, followed by subsequent 2D-MHP formation ($n = 1$ and 2 with PEABr) to achieve

S. Ramakrishnan, D. Song, Y. Xu, X. Zhang, G. Aksoy, Q. Yu
Robert Frederick Smith School of Chemical and Biomolecular Engineering
Cornell University
Ithaca, NY 14853, USA
E-mail: qy10@cornell.edu
M. Cotlet, M. Li, Y. Zhang
Centre for Functional Nanomaterials
Brookhaven National Laboratory
Upton, NY 11973-5000, USA

The ORCID identification number(s) for the author(s) of this article can be found under https://doi.org/10.1002/aenm.202302240

DOI: 10.1002/aenm.202302240

excellent PCEs of 24.7% with an exceptional V_{oc} of 1.20 V.[18] In contrast, La-Placa and Sidhik et al. report inferior device performance arising from misaligned energy levels among the conduction band minimum (CBM) of 2D- and 3D-MHP and the lowest unoccupied molecular orbital (LUMO) of the electron transport layer (ETL), with significant electron blocking by the phase-pure 2D-overlayers up to $n = 3$, even for low capping thicknesses below 8 nm.[19,20] Thus, weakening the degree of quantum-confinement of the 2D-MHP layers and fine-tuning the energy alignment at the 3D/2D/ETL interfaces to allow electron tunneling to the ETL remains a longstanding issue.

The degree of quantum-confinement may be reduced by manipulating the number of octahedral layers n because the energy landscape of 2D-MHPs is significantly narrowed for larger n values (n = 3 and 4).[1,3,21] A majority of previous research has focused on identifying specific ligands to form suitably larger n fragments by tuning the reactivity, steric hindrance, and atomic radius of the ligand in conjunction with suitable post-treatment.[22–25] More critically, Chen et al. reveal rational solvent selection as the key to manipulating 2D-MHP distribution through the inclusion of excess methylammonium iodide (MAI) and dimethylformamide (DMF) in the ligand solution to generate greater density of MA^+ and PbI_2, indeed paving the way for tuning n of 2D-MHPs in p–i–n solar cells. As such, the ligand species used and the solvent properties (e.g., polarity and interaction with 3D-MHP) decide the arising phase-formation behavior.[26] However, most of these works employ solvents that irrevocably damage the 3D-MHP surface (e.g., isopropanol (IPA)) as the ligand processing solvent of choice. Recently, it was revealed that IPA reconstructs the 3D-MHP surface into a relatively more PbI_2-rich state during post-treatment.[27] The shallow iodide defects thus formed lower the activation barrier for perovskite transformation into a non-photoactive phase.[28] Therefore, it is necessary to expand the library of processing solvents with a view of understanding the solvent interaction on the 3D-MHP surface termination to favorably drive the growth of larger n 2D-MHPs.

Furthermore, most recent works are limited to the RPP analog of 2D-MHPs, which feature highly anisotropic charge carrier transport with charge carrier mobilities across the bulky organic ligands (out-of-plane) being magnitudes smaller than the in-plane counterpart along the $[PbX_6]^{4-}$ framework.[29] RPPs are also characterized by a Van der Waal gap between ligands, with a substantial charge tunneling barrier across adjacent $[PbX_6]^{4-}$ frameworks (>10 Å).[5,30] These shortcomings are accentuated by the tendency of 2D-MHPs to adopt a horizontal or mixed orientation on top of the 3D-MHPs.[18] DJPs, as a less investigated structural analogue of 2D-MHPs, offer possibilities to diminish the effect of quantum-confinement.[31] The diammonium ligands templating DJPs bring the adjacent $[PbX_6]^{4-}$ frameworks closer, well within the range of charge tunneling through the insulating ligands (c.a. 4 Å), and facilitating relatively more symmetric charge transport.[32]

In this paper, we investigate the formation mechanisms of 2D DJP on 3D-MHP heterostructures. We find that the formation dynamics and n of 2D-MHP capping layers are inextricably tied to the solvent-induced surface reconstruction of the underlying 3D-MHP. Isopropanol (IPA) reconstructs the 3D-MHP surface into a PbI_2-rich state, while 2, 2, 2-trifluoroethanol (TFE) inflicts almost no damage, preserving the FA/MA-rich surface. In situ x-ray scattering reveals that 2D/3D formation with IPA-based solvent mixtures proceeds via the initial formation of a smaller n strata, followed by a sparse substratum of larger n, while TFE leads to nucleation of larger n first and smaller n last, uniformly distributed across the 2D-MHP cross-section. In addition, the abundance of nucleation sites created during surface reconstruction by IPA presents a diffusion barrier for 2D-MHP formation, severely hindering the growth of larger n, while fewer nucleation sites during TFE treatment allows uniform ligand distribution, leading to 2D-MHP growth dominated by $n \geq 3$. Based on these insights, we fabricated 2D/3D heterostructures based on RPP and DJP capping layers via synergistic solvent and ligand engineering to tailor the energy landscape of p–i–n solar cells. Proof-of-concept 2D/3D films dominated by $n \geq 3$ based on 3-aminomethylpyridinium diiodide (3-AMPY) DJPs exhibit very long electron diffusion lengths up to 4 µm compared to their RPP analogs. Simultaneously, the DJPs enable favorable CBM alignment at the 3D/2D/ETL interfaces, with significantly reduced quantum-confinement and barrier to electron transport. Inverted 2D/3D PSCs based on 3-AMPY and TFE-based solvents achieve a champion power conversion efficiency of 23.60% with a remarkable V_{oc} and FF of 1.19 V and 84.5%, respectively. Furthermore, the defect-free capping layers produced via TFE treatment benefit from the favorable energy landscape, strong electrostatic bonding and structural integrity of DJPs to achieve superior stabilities with t_{92} of 1440 h under ambient conditions (RH = 50–60%) and t_{94} of 960 h at 85°C.

2. Results and Discussion

2.1. Ligand Effect on the Energy Landscape of 2D-MHPs

The major hurdle toward the development of 2D/3D p–i–n PSCs lies in the upshifted CBM of the quantum-confined 2D-MHP capping layer. A 2D-MHP capping layer with $n > 2$ phases with reduced quantum-confinement should be beneficial to PCE via simultaneous defect passivation and improved charge carrier transport. The quantum-confinement may also be modulated by rational bulky organic ligand selection. **Figure 1**a displays representative RPP and DJP phases, where RPPs have two layers of interdigitating ligands held by weak Van der Waal forces, while DJPs have a single layer of ligands separating the inorganic octahedral frameworks. The ligands influence the crystal configuration and interlayer spacing of inorganic octahedral frameworks on many levels, depending on the charge, functional group position, and steric effects.[33] These parameters, particularly the octahedral distortion and framework-to-framework interlayer spacing, should have a profound impact on the electronic structure.[33] Accordingly, the DJP-forming ligands 3-aminomethylpyridine (3-AMPY) and 4-aminomethylpyridine (4-AMPY) were shortlisted as possible ligands for 2D-MHP capping layer due to their narrow interlayer spacing and lower octahedral distortion versus RPP-forming phenylethylamine PEA (Figure 1b).

To visualize their band structure with respect to 3D-MHPs, we performed ultraviolet photoelectron spectroscopy (UPS) on thin films of RPP and DJP with PEA and 3-AMPY as ligands, respectively (Figure 1c). Thin films were fabricated by first preparing single crystals of phase-pure n = 3 $(PEA)_2MA_2Pb_3I_{10}$ and

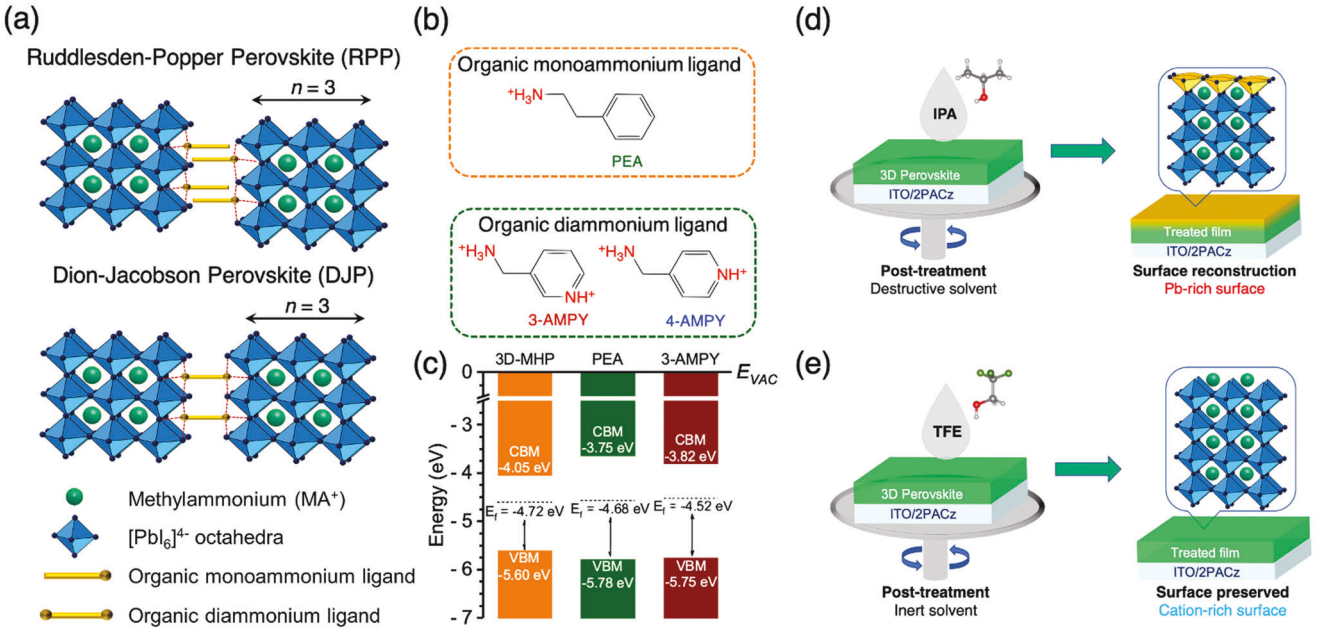

Figure 1. a) Schematic representation of $n = 3$ 2D RPP and DJP. b) The three ligands used to prepare 2D/3D heterostructures in this study: RPP-forming PEA and DJP-forming 3-AMPY and 4-AMPY. c) The UPS measured band levels of representative 3D-MHP and $n = 3$ 2D RPP and DJP illustrating the effect of reducing quantum confinement via forming 2D DJP on the CBM. d,e) Schematics representing the impact of destructive IPA solvent and inert TFE solvent on 3D-MHP surface.

(3-AMPY)$MA_2Pb_3I_{10}$ and translating their purity into thin-films. (Refer to Note S1 and Figure S1, Supporting Information). As expected of quantum-confined structures, the valence band maximum (VBM) and CBM are noticeably offset from those of the 3D-MHP. A shorter halide–halide interlayer distance should lead to a greater degree of antibonding, pushing up the VBM. Accordingly, the VBM of the 3-AMPY 2D DJP film is shifted upward by c.a. 0.03 eV compared to the PEA RPP film. Estimating the CBM position using the optical bandgap (2.03 eV for PEA and 1.93 eV for 3-AMPY, Figure S1b, Supporting Information) yielded CBM values of −3.75 and −3.82 eV for $n = 3$ PEA and 3-AMPY 2D-MHP films, respectively. The downshifted CBM of 3-AMPY DJP is consistent with the reduced octahedral distortion of $n = 3$ 3-AMPY DJP. [31] A reduced octahedral distortion can provide new hybrid orbitals via *s* and *p* halide orbital hybridization, pushing down the CBM.[34] While the reduced CBM of 3-AMPY DJP certainly displays a noticeable offset compared to the 3D-MHP, the smaller degree of CBM offset and shorter interlayer distance should benefit electron tunneling compared to the RPP analog. A thin capping layer (c.a. 10–20 nm) dominated by $n \geq 3$ DJPs should take advantage of both factors to realize efficient p–i–n PSCs.

2.2. Solvent-Mediated 3D-MHP Surface Reconstruction

To leverage the reduced electron transport barrier of DJPs toward efficient p–i–n PSCs, we sought to design surface treatments driven toward the preferential formation $n \geq 3$ phases atop a 3D template. One of the critical considerations toward the phase formation tendency of 2D/3D-MHPs lies in the surface composition prior to 2D-MHP formation, which is inextricably linked to the interaction between perovskite and the ligand processing solvent.[18,24,27] Conventionally, most studies have employed isopropanol (IPA) to great effect due to its ability to dissolve a broad window of ligands.[12,26] However, IPA tends to leach off small organic cations (MA^+, FA^+) to reconstruct the 3D-MHP surface into a relatively PbI_2-rich state (Figure 1d) during post-treatment, with a very unstable and reactive surface.[27] The PbI_2-terminated surface has a heightened binding affinity for 2D-MHP forming ligands, leading to a rapid and uncontrolled reaction almost ubiquitously forming $n = 1$ and 2 in the majority.[27,35] Furthermore, the post-treated surface tends to possess FA/MA-vacancies, which generate defects and facilitate 3D-MHP degradation.[28] On the other hand, solvents with weak interaction with 3D-MHPs (e.g., chloroform (CF)) allow ligand deposition onto an intact 3D-MHP surface (Figure 1e).[36] The spontaneous cation exchange between deposited ligands and FA^+/MA^+ that constitute the surface termination[27,37] leads to progressive dimensional reduction by initially forming larger *n* intermediates (from $n = 3 \rightarrow 2 \rightarrow 1$).[38] Thus, we hypothesize that regulating the surface composition by tuning solvent interaction with 3D-MHP and interrupting the dimensional reduction should afford large *n*. However, the applicability of CF is severely hindered by the solubility window being limited to predominantly long aliphatic ammonium salts.[34] Thus, we turned to screen alternative solvent combinations that have a weak affinity for 3D-MHP surface while still dissolving 3-AMPY and 4-AMPY ligands to fabricate the desired DJP/3D-MHP heterostructures with large *n*.

Fluorinated solvents possess a weaker solvation effect than their non-fluorinated counterparts. In particular, 2, 2, 2-trifluoroethanol (TFE) is a protic solvent with very strong hydrogen bond donating ability but weaker electron pair donation

due to the highly electronegative -CF_3 group (Figure 1e). Consequently, TFE has a strong solvation effect on anions, while weakly solvating cations. Thus, we anticipated that TFE as a ligand solvent would lead to less pronounced surface reconstruction and low FA^+/MA^+ leaching while still possessing sufficient polarity and dielectric constant necessary to dissolve the ligands salts in Figure 1b. As TFE is a more polar solvent than IPA, the penetration by the solvent into the 3D-MHP film should be greater, allowing a more uniform distribution of ligands into the 3D-MHP grain boundaries. Thus, we investigated the 3D-MHP surface reconstruction effect of triple-cation $Cs_{0.03}(FA_{0.90}MA_{0.10})_{0.97}PbI_3$ 3D-MHP films exposed to neat IPA and TFE by analyzing the carrier lifetime and spectral properties using time-resolved photoluminescence (TRPL) and static photoluminescence (PL). Films subjected to a brief exposure to IPA exhibit slightly lower carrier lifetimes and PL intensity compared to pristine while TFE-exposed films remain almost no changes (Figure S3, Supporting Information). Additionally, to mimic scaled-up fabrication conditions, we immersed 3D-MHPs in IPA and TFE for a period of 24 h. Ostensibly, the 3D-MHP immersed in IPA forms a golden-yellow film surface, indicating the formation of a PbI_2 or δ-$FAPbI_3$-rich surface with pronounced surface reconstruction. In contrast, the TFE-immersed film displays very little change in appearance (Figure S4, Supporting Information).

We included a trace quantity of polar, coordinating solvent (DMF) to generate free octahedra and allow deeper penetration of ligands into the 3D-MHP.[26] To evaluate the leaching capability of solvent mixtures with 0.5 vol.% of DMF, we spin-coated 100 µL neat IPA:DMF and TFE:DMF onto a 3D-MHP film. Scanning Electron Microscopy (SEM) revealed that the surface of the 3D-MHP was completely reconstructed into bright platelets, which are likely PbI_2 crystallites,[39] with significant phase segregation upon IPA:DMF washing (Figure S5b, Supporting Information). However, the morphology of the pristine film and TFE:DMF-treated film are comparable, indicating minimum structural damage (Figure S5a,c, Supporting Information). In addition, we studied the PL distribution across the film surface using confocal photoluminescence mapping (CPLM). Figure S6a (Supporting Information) exhibits the CPLM of a typical 3D-MHP, with alternating bright domains at the center of a single grain and dark domains at the grain boundaries. In contrast, the overall PL intensity of IPA:DMF washed films is bleached tremendously, characteristic of a defect-riddled surface with significant non-radiative recombination (Figure S6b, Supporting Information). TFE:DMF washing, on the other hand, elicits comparable emission characteristics to the pristine 3D-MHP (Figure S6c, Supporting Information). Lastly, the X-ray diffraction patterns collected from the three representative films exhibit a noticeable PbI_2 peak in the case of IPA:DMF treated film compared to the TFE:DMF washed and pristine 3D-MHP film (Figure S7, Supporting Information). Overall, the results collectively report the destructive nature of the IPA:DMF mixture by generating a relatively PbI_2-rich surface and the relatively inert nature of the TFE:DMF mixture toward maintaining a relatively unharmed FA^+/MA^+-rich 3D-MHP surface. The above dichotomy in the surface types manifests remarkable differences during 2D-MHP formation.

2.3. In Situ GIWAXS of 2D-MHP Formation During Spin-Coating and Annealing

We employed in situ grazing-incidence wide-angle x-ray scattering (GIWAXS) measurements to derive insights into the influence of solvent mixture on the film evolution of 2D/3D heterostructures. To achieve this, we spun a glass/$Cs_{0.03}(FA_{0.90}MA_{0.10})_{0.97}PbI_3$ 3D-MHP film at 2000 rpm and discharged a ligand solution (2 mg/mL 3-AMPY, 2 mg/mL of MAI and 0.5 vol% DMF in IPA or TFE) at c.a. 1.6 s (Figure S8, Supporting Information). We emphasize that MAI was introduced to all ligand solutions in this work to allow larger n formation unless explicitly stated. For brevity, the solutions and 2D/3D heterostructures fabricated using 3-AMPY as the bulky organic ligand and IPA:DMF or TFE:DMF as the ligand solution will be dubbed 3-AMPY (IPA:DMF) and 3-AMPY (TFE:DMF) and vice versa.

Heatmaps of azimuthally integrated in situ GIWAXS patterns, circularly-averaged linecuts, intensity of relevant DJP peaks over time and representative GIWAXS timestamps are displayed in **Figure 2**a–h, for 3-AMPY (IPA:DMF) and 3-AMPY (TFE:DMF), respectively. Before the discharge of ligand solution, a strong peak prevails at 0.97 $Å^{-1}$ (Figure 2a,e), corresponding to 3D-MHP. When IPA:DMF is employed in ligand solution, two broad halos are observed at 0.80 and 1.43 $Å^{-1}$ along the q_z-axis immediately upon solvent exposure (Figure 2a; Figure S9a, Supporting Information), corresponding to δ-$FAPbI_3$ and isopropanol solvent, respectively.[27,35] Typically, δ-$FAPbI_3$ was formed in systems when 3D-MHPs are dipped into IPA baths containing FAI or ligands, precluding the degradation of 3D-MHP into PbI_2. Immediately after solvent evaporation (3.6 s), the 3D-MHP peak displays a pronounced drop in intensity, implying surface reconstruction of the 3D-MHP. Figure 2a,c,d show that after complete solvent drying, scattering peaks appear at $q = 0.38$ $Å^{-1}$ ($d \approx 16.52$ $Å^{-1}$) at an initial time scale at ≈4 s, corresponding to $n = 2$ (3-AMPY)$MAPb_2I_7$ phase. After a substantial delay of ~5 s, a weaker peak corresponding $n = 3$ ($q = 0.28$ $Å^{-1}$, $d \approx 22.35$ Å) appears (Figure 2a,c).[31] Thus, $n = 3$ formation only occurs after the termination of the $n = 2$ DJP. A peak at $q = 0.45$ $Å^{-1}$ ($d \approx 14$ Å) that grows concurrently with $n = 3$ also appears, corresponding to the (040) diffraction of $n = 4$ (Note S2, Supporting Information). The GIWAXS timestamps during spin coating in Figure 2d show that all diffraction peaks of 2D-MHPs are strongly centered at $q_x = 0$ $Å^{-1}$, implying that the DJPs thus formed adopt a parallel orientation to the glass substrate. It is noteworthy that supplementing MAI in the ligand solution has led to total suppression of $n = 1$ (3-AMPY)PbI_4 phase. Indeed we note the formation of the corresponding $n = 1$ or $n > 2$ phase for 2D/3D heterostructures fabricated using a ligand solution composed of 3-AMPY and IPA:DMF without MAI or DMF, respectively (Figure S11b,c, Supporting Information).

The in situ GIWAXS revealed striking differences when processed using TFE:DMF, as displayed in Figure 2f–h. Immediately upon ligand solution discharge, we observed only a single halo centered at the q_z-axis at 1.42 $Å^{-1}$ ($d = 4.42$ $Å^{-1}$) representing TFE solvent (Figure S9b, Supporting Information), again reiterating that TFE-based solvents do not reconstruct the 3D-MHP surface. Figure 2e–h show that at ~8 s, faint scattering peaks centered at $q_x = 0$ $Å^{-1}$ come to the fore at $q = 0.45$ $Å^{-1}$,

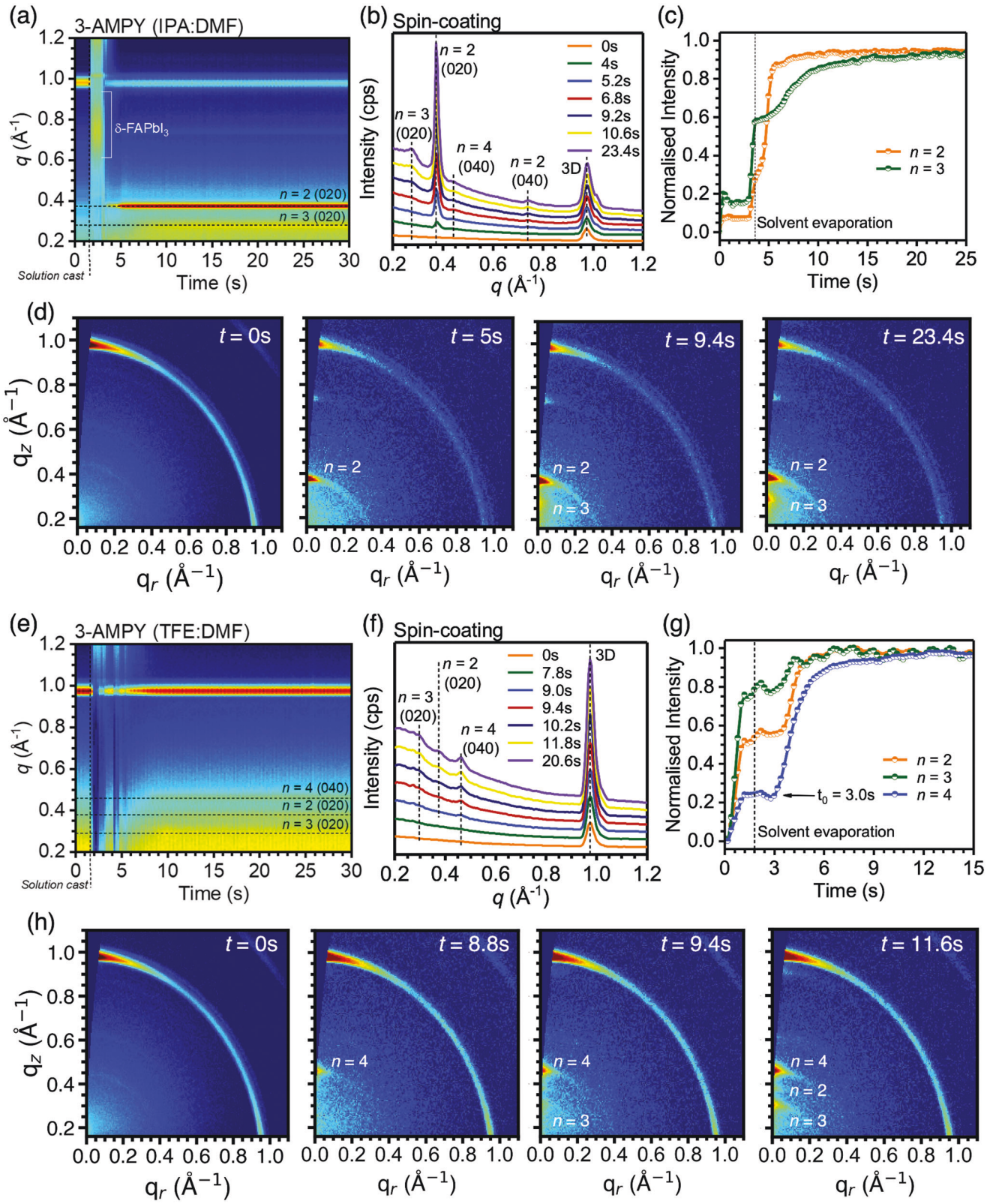

Figure 2. a,e) Azimuthally-integrated in situ GIWAXS heat map during spin-coating, b,f) circularly-averaged linecuts, c,g) the temporal evolution of relevant 2D-MHP peaks, d,h) individual GIWAXS heat maps at representative timestamps for as-spun films of 2D/3D films post-treated using 3-AMPY + MAI (2 mg mL^{-1} each) in a–e) IPA:DMF and f–i) TFE:DMF, respectively. A grazing-incidence angle of 0.15° was maintained throughout the in situ GIWAXS experiment.

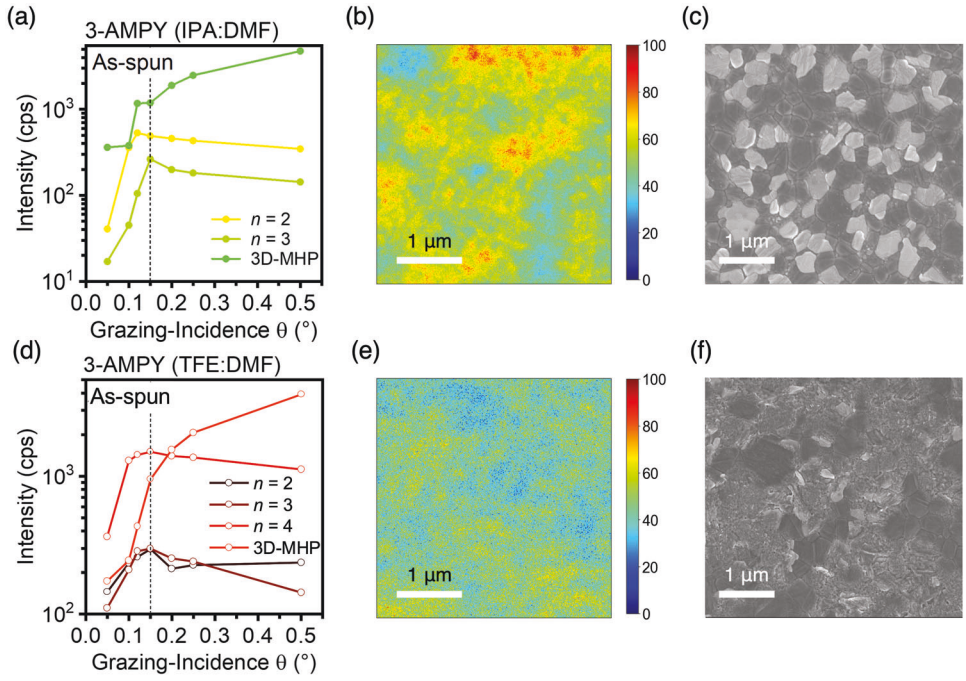

Figure 3. a,d) Ex situ GIWAXS intensity of 2D-MHPs and 3D-MHP extracted via area-integrated peaks of n as a function of grazing-incidence angle with the critical angle (0.15°) marked as a dashed line, b,e) confocal photoluminescence mapping (CPLM) with 400 nm excitation and a 700 nm short-pass filter and c,f) topological SEM images of as-spun 3-AMPY (IPA:DMF) a–c) and 3-AMPY (TFE:DMF) d–f) 2D/3D heterostructures thin-films.

corresponding to (040) diffraction of $n = 4$ (3-AMPY)$MA_3Pb_4I_{13}$ phase, with $n = 3$ phase in close succession at $q = 0.28$ Å^{-1} (Figure 2g). Similar to IPA:DMF, the GIWAXS timestamps (Figure 2h) reveal that the DJPs adopt a parallel orientation with respect to the substrate. The peak corresponding to the $n = 2$ phase appears 0.8 s later. While the onset for crystallization is slower in the case of TFE:DMF solvent as compared to IPA:DMF, the sequential appearance of different n phases is considerably faster. Furthermore, in stark contrast to the IPA:DMF sample where 2D-MHP formation progressed via $n = 2 \rightarrow 3 \approx 4$ formation, TFE:DMF-treated samples exhibit the opposite trend with $n = 4 \rightarrow 3 \rightarrow 2$. Contrastingly, Sargent et al. report the dimensional reduction from an initially $n = 3$ rich state to a final pure $n = 1$ state via interconversion of 2D-MHP phases for a VBABr-based RP 2D/3D heterostructures processed from an inert solvent CF:IPA (97:3 v/v).[38] As Dion-Jacobson analogues possess stronger electrostatic bonds and a rigid lattice, they are more resilient to subsequent bifurcation/growth by 3-AMPY or MAI intercalation.[40]

We explain the trends and sequence of 2D-MHP formation through isothermal classical Avrami analysis (Figure S12, Supporting Information).[41–44] IPA:DMF samples display an interface-limited crystallization pathway during the early stage formation of $n = 2$ DJPs, followed by the diffusion-limited formation of $n = 3$ DJPs (Figure S12a, Supporting Information). Based on the IPA:DMF-induced surface reconstruction, we reasoned that during post-treatment, a large number of nucleation sites (PbI_2) are formed on the 3D-MHP surface. Thus, the rate limiting steps to 2D-MHP formation were the initial physisorption of ligands or MAI to the 3D-MHP surface, rapidly forming $n = 2$ and the subsequently limited diffusivity of ligands across the solid bulk of the $n = 2$ DJP (Figure S12a and Note S3, Supporting Information). In contrast, TFE:DMF solvents do not leach the surface cations, presenting very few nucleation sites for the ligands, causing site-saturation (Figure S12b and Note S3, Supporting Information). As a result, ligand physisorption is limited in comparison, leading to a more uniform ligand distribution across both the 3D-MHP surface and grain boundaries, causing nearly simultaneous formation of large n DJPs as seen in Figure 2e.

To understand the divergent compositional and temporal evolution of the 2D/3D film formation with different ligand solvents, we studied the film structure of the 2D/3D films immediately after spin-coating without further post-treatment (hence dubbed as-spun). To probe the 2D-DJP composition along the cross-section of the film, we employed angle-dependent ex situ GIWAXS at grazing-incidence angles between 0.05 to 0.50°, at a critical angle of 0.15° (**Figure 3**a,b). The penetration depth as a function of the grazing-incidence angle is calculated and shown in Figure S14 (Supporting Information). We also performed confocal photoluminescence mapping (CPLM) to selectively observe the photoemission of all 2D-DJPs present in the film (Figure 3b,e) and correlated the observations with SEM (Figure 3c,f).

Figure 3a reveals that the overall intensity of $n = 2$ was found to exceed that of $n = 3$ irrespective of the grazing-angle, indicating a film dominated by $n = 2$. However, the integrated area of $n = 2$ sharply increases at lower grazing-incidence angles (i.e., shallower penetration depth) compared to $n = 3$ and 3D-MHP peak intensity before reaching a maximum at an angle of 0.12° (5 nm X-ray penetration) and becoming invariant thereafter. In contrast, $n = 3$ increased gradually before reaching a maximum at 0.15° (≈14 nm). As noted in Figure S14 (Supporting Information), the x-ray penetration depth sharply increases between 0.12

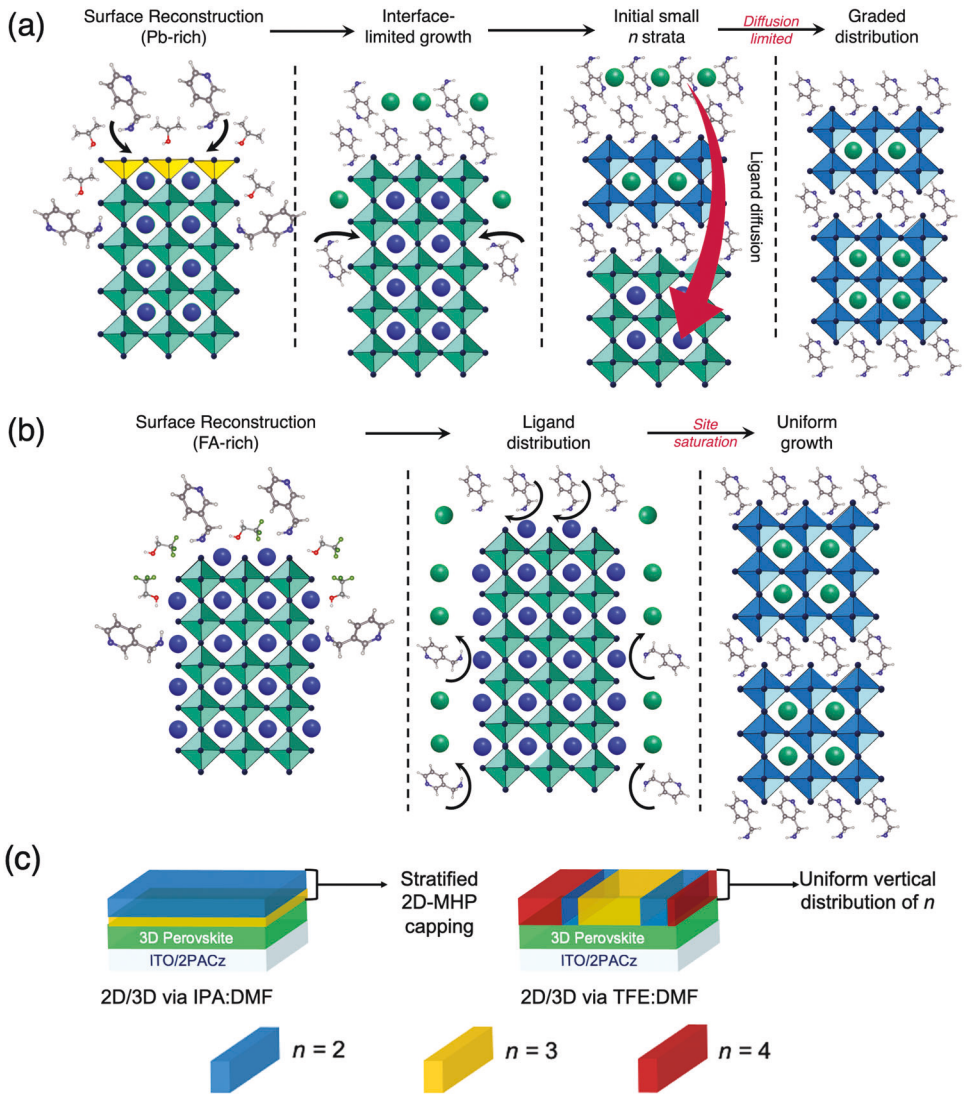

Figure 4. Proposed mechanism depicting surface reconstruction, ligand distribution and 2D-MHP growth in case of a) 3-AMPY (IPA:DMF) and b) 3-AMPY (TFE:DMF). c) Schematic depicting the film structure of as-spun 2D/3D heterostructures fabricated using ligand solutions based on IPA:DMF and TFE:DMF.

to 0.15° (by ≈10 nm). We infer that the 2D-DJP formation occurs predominantly due to an initial rapid surface physisorption of ligands onto the PbI_2-termination on the reconstructed 3D-MHP interface, forming a strata of $n = 2$, followed by ligand diffusion deeper into the film via the grain boundaries to form a substratum of $n = 3$, forming a graded 2D-MHP capping layer.[45] CPLM (Figure 3b) revealed that the majority of the emission of the 2D-DJPs in the 3-AMPY (IPA:DMF) sample arises from the central portion of grains and less from the boundaries, with the 2D-DJPs getting distributed as platelets on the 3D-MHP surface.

In contrast, Figure 3d shows that the as-spun 3-AMPY (TFE:DMF) samples display a very different film structure, with the peak intensities of $n = 2$, 3, and 4 phases reaching the maxima at the same angle at 0.15° (≈14 nm) and becoming invariant thereafter. We infer that the n = 2–4 2D-DJPs are permuted across the top film surface in mixed domains that extend downward. The CPLM results (Figure 3e) support this, displaying a more uniform emission throughout the film surface, with comparable PL intensity between the grain boundaries and the perovskite grains. A similar effect was previously reported for ethanol as solvent.[46] The SEM image (Figure 3f) shows merged and indistinct grain boundaries between 3D-MHPs as a result of 2D-MHPs penetrating deeper into the film microstructure. Thus, TFE:DMF solvent allows a more uniform ligand distribution across the film surface and deeper penetration into grain boundaries, fortifying the 3D-MHP surface. In addition, we found that IPA:DMF and TFE:DMF produce 2D-capping layers of comparable thicknesses for the same ligand concentrations (Figure S14b,c, Supporting Information), as both heterostructures reach maximum intensity at the same grazing-incidence.

Taken collectively, we propose the following formation mechanisms of 2D-DJP on 3D-MHP with IPA:DMF and TFE:DMF solvents in **Figure 4**a,b, respectively. The formation of 2D-MHPs with IPA:DMF is precluded by an intermediate state induced by

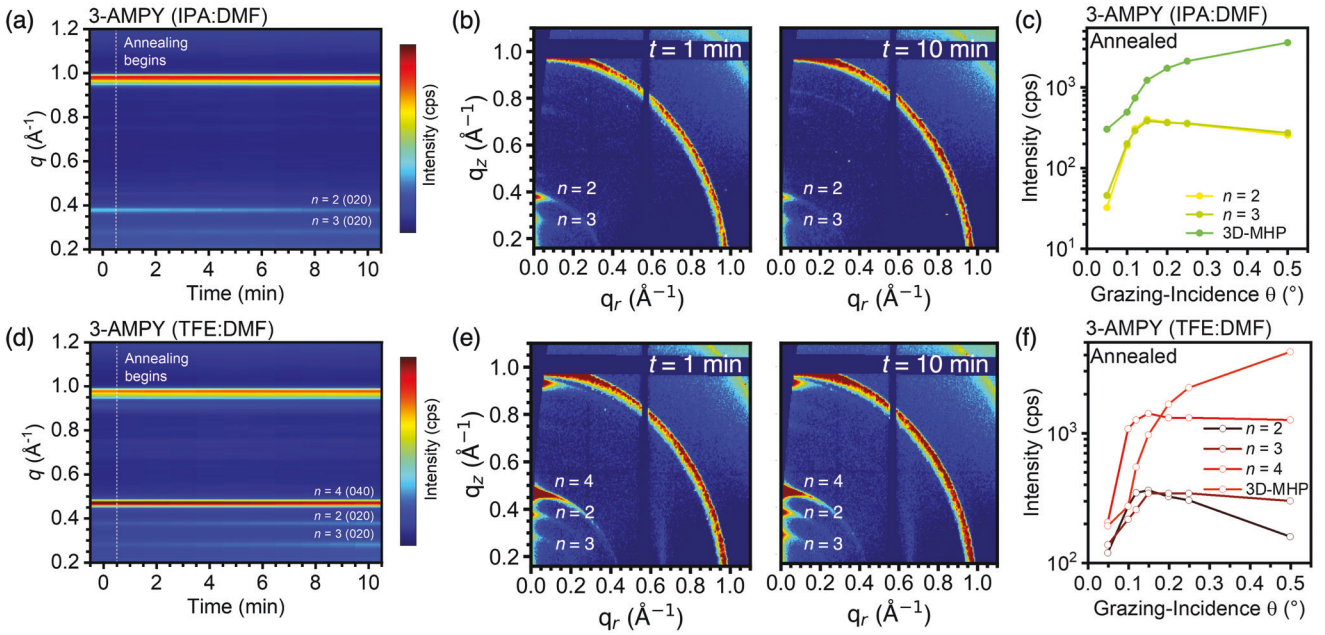

Figure 5. a,d) Azimuthally-integrated in situ GIWAXS heat map during thermal annealing with the critical angle (0.15°) marked as a dashed line, b,e) individual GIWAXS heat maps at representative timestamps and c,f) GIWAXS scattering intensity of 2D-MHPs and 3D-MHP extracted via area-integrated peaks of dominant *n* as a function of grazing-incidence angle of annealed a–c) 3-AMPY (IPA:DMF) and d–f) 3-AMPY (TFE:DMF).

cation leaching by destructive solvents, leading to a reconstructed δ-$FAPbI_3$/ PbI_2-rich surface. The δ-$FAPbI_3$ and PbI_2 serve as nucleation sites for rapid ligand anchoring via physisorption and subsequent 2D-MHP crystallization, as ligand-terminated perovskite surfaces are thermodynamically favored compared to small- cation-termination (Figure 4a).[47] Eventually, a finite strata of small *n* (in case of 3-AMPY, $n = 2$) is formed on the reconstructed surface via interface-limited crystallization. In sequence, a slower diffusion-limited secondary growth occurs at the lower 2D-MHP/3D-MHP interface, leading to the crystallization of $n \geq 3$. We speculate the ligand-terminated dense small *n* impede cation diffusion (3-AMPY, MAI) by self-assembly of another layer of unreacted ligands, causing a noticeable time delay in the formation of a sparse larger *n* strata. The initial surface anchoring and fast reaction of ligands to form small *n* renders the formation of larger *n* difficult due to the overconsumption of ligands.

On the other hand, solvent combinations with TFE:DMF do not reconstruct the 3D-MHP surface into a PbI_2-rich state with negligible changes in surface composition (Figures S5 and S9b, Supporting Information). Consequently, very few nucleation sites are available for the bulky ligands to bind on to, favoring uniform ligand distribution at the 3D-MHP surface and grain boundaries with limited physisorption. A downward 2D-DJP formation occurs at roughly the same time scale with different *n* until the ligands are completely consumed via cation exchange, leading to domains of different *n* along the cross-section of the 2D-MHP capping layer. Additionally, the inert nature of the TFE:DMF treatment coupled with the relatively low concentration of ligands produced a relatively larger density of $n = 3$ and 4 with minimal damage to the 3D-MHP.

To explore the proposed mechanism in a broader context, we also investigated the formation dynamics of 4-AMPY, a structural isomer of 3-AMPY, for DJP and the more common PEA ligand for RPP (Figures S15a,b and S16a,b, and Note S5, Supporting Information). The emergent formation dynamics in Figures S15a,b and S16a,b (Supporting Information) confirm that the solvent interaction with the 3D-MHP plays a more crucial role in regulating the surface reconstruction and nucleation sites on the 3D-MHP, dictating the sequence of formation of *n* and relative density of different *n*-valued 2D-MHPs (Figure 4a,b; Figures S15 and S17, Supporting Information).

If unreacted ligand diffusion poses a barrier to the formation of 2D/3D heterostructures, annealing should elicit changes in film structure and composition compared to Figure 3a,d.[48,49] To clearly identify the existence of a possible diffusion-limited formation mechanism in 2D/3D heterostructures, we subjected the as-spun 3-AMPY-treated films to accelerated annealing at RH = 40–50% and T = 130 °C immediately following spin-coating. **Figure 5** display the heatmaps of azimuthally integrated in situ GIWAXS patterns over an annealing period of 10 min, 2D-GIWAXS patterns at specific timestamps and angle-dependent GIWAXS of dominant *n* DJPs at the end of the annealing experiment.

In Figures 5a,b, annealing the 3-AMPY (IPA:DMF) film enabled a transition from a relatively $n = 2$ rich film into a film with an almost equal density of $n = 2$ and 3 phases. The intensity of $n = 2$ (020) peak gradually decreases over the 10 min period, while the $n = 3$ (020) and $n = 4$ (040) peaks remain unchanged (Figure S18a,c, Supporting Information). Annealing affords the activation energy required to not only facilitate cation exchange leading to intermixing between $n = 2$ and 3 phases but also the diffusion of unreacted salts (MAI, 3-AMPY) deeper into the perovskite film (via grain boundaries).[49] On the other hand, annealing induces structural reorganization in 2D-MHP phase and

distribution (Figure 5c). The intensity of both $n = 2$ and 3 rises in tandem at a similar rate, before becoming invariant at 0.15° (≈14 nm). Evidently, post-annealing transforms the graded phase distribution (Figure 3a) into a uniform mixture of $n = 2$ and 3 phases scattered across the 2D-DJP capping layer.

In Figures 5d,e, annealing the TFE:DMF-treated samples results in minimal change in intensity to $n = 4$ phase, but a gradual increase to $n = 3$ and 2 phases. There is no degradation of the so-formed 2D-MHPs into new lower n polymorphs (Figure 5d; Figure S16b,d, Supporting Information), whereas Figure 5f shows that the integrated areas of as-annealed 3-AMPY (TFE:DMF) samples exhibit a similar film structure to the as-spun sample with the phases becoming invariant at 0.15° (≈14 nm). We infer that the $n = 2$–4 2D-DJPs are uniformly permuted across the height of the film surface in mixed domains with $n = 2$–4. These trends imply more effective mixing and utilization of ligands to form 2D-MHPs as early as the spin-coating stage. Thus, the 3-AMPY (TFE:DMF) films are dominated by $n = 3$ and 4 that extend downward onto the 3D-MHP interface (Figure 4c, right panel). The energy landscape and reduced compositional drift at elevated temperatures with 2D-MHP capping layer concentrated at $n = 3$ and 4 should be more favorably disposed toward sustained electron tunneling under extrinsic stressors.

2.4. Influence on Photophysics and Recombination Dynamics

Rational solvent selection has thus allowed regulation of 3D-MHP surface termination and nucleation sites to guide the 2D-MHP distribution atop a 3D-MHP template. To close the loop between surface-termination, formation dynamics and translatability to superior solar cell figures of merit, we investigated the implication of solvents and 3D-MHP leaching on the charge transport in PEA, 4-AMPY and 3-AMPY treated films. The extent of solvent-induced leaching of 3D-MHP during the 2D/3D formation is expected to have a noticeable impact on the carrier dynamics of arising films. Static photoluminescence (PL) of representative films on a glass substrate reveals a profound difference between films processed using IPA and TFE. Irrespective of solvent, all 2D/3D films show an appreciable increase in PL signal compared to the pristine 3D-MHP counterpart, with reduced non-radiative recombination (**Figure 6**a–c). However, only TFE:DMF films fully leverage the defect passivation effect of 2D-MHPs by avoiding leaching of the FA^+/MA^+ during the 2D-treatment to form surfaces with lower non-radiative recombination, bringing forth enhanced PL emission.[37] In addition, DJP ligands also engender a larger degree of PL enhancement compared to the RPP counterpart due to superior charge transport and reduced quantum-confinement (Figure 6b,c).[50] 4-AMPY treatment brought about a three-fold PL signal enhancement, while 3-AMPY increases five-fold, implying dramatic suppression of non-radiative recombination.[51] A similar trend is apparent in the time-resolved photoluminescence spectra (TRPL), where longer average lifetimes were recorded for DJP heterojunctions based on TFE:DMF ligand solutions (Figure 6d,e; Figure S19a,c, Supporting Information). We analyzed the decay kinetics of the films as a superposition of fast (τ_1) and slow (τ_2) recombination dynamics (Table S2, Supporting Information). The fast recombination dynamics are associated with trap-assisted surface recombination, while the slower dynamics are attributed to radiative recombination within the bulk perovskite.[24,51] In agreement with the PL enhancements in Figure 6a–c, the TFE:DMF treated films unanimously display a prolonged surface recombination lifetimes τ_1 in comparison to their IPA:DMF counterparts, indicating that the latter possesses a certain degree of non-radiative recombination at the 2D-capping interface, possibly due to defect formation and larger density of $n = 2$ phases.[52] Most uniquely, 3-AMPY-based films demonstrate a monoexponential decay compared to 4-AMPY and PEAI (Figure S19a,c respectively and Table S2, Supporting Information), with a long average lifetime τ_{ave} of 1374 and 1738 ns with IPA:DMF and TFE:DMF, respectively, indicating a significant reduction in surface trap states and efficient passivation.

To verify the translatability of these insights to p–i–n PSCs, we studied the degree of PL quenching and electron diffusion length when an ETL ($PC_{61}BM$) is deposited atop the films. The 2D/3D films have a strong degree of PL quenching compared to the pristine 3D-MHP films (Figure 6e; Figure S19b,d, Supporting Information). The diffusion length for electrons can be evaluated by comparing the slow recombination dynamics τ_2 of the quenched and pristine films. The quenched carrier lifetimes and diffusion length values are summarized in Table S3 (Supporting Information). The approximate value of diffusion length L_D was estimated using the following equation suggested by Snaith et al:[53]

$$L_D = \frac{2d}{\pi}\sqrt{2\left(\frac{\tau_2}{\tau_{2,\ quenched}} - 1\right)} \quad (1)$$

The pristine 3D-MHP has an electron diffusion length of 1162 nm, which is typical for a triple-cation perovskite film. In comparison, 2D/3D heterostructures exhibit an elongated electron diffusion length (Figure 6f). The 3-AMPY (IPA:DMF) and 3-AMPY (TFE:DMF) films demonstrate nearly three-fold and four-fold enhancement of electron diffusion lengths at 2831 and 3996 nm, respectively. Overall, these measurements validate that due to the stratified nature of 2D/3D films via IPA:DMF treatment and the presence of $n = 2$ phases, the electron diffusion length is lower than that of the TFE:DMF sample which contains a uniform vertical n distribution with larger density of $n > 2$ phases.

As the surface phase composition has a profound impact on the charge transfer between 2D and 3D-MHPs, we performed femtosecond transient absorption spectroscopy (TAS) on the 3D-MHP and 2D/3D films to accurately identify the phase distribution of different 2D capping layers.[24,26] Figures 6g,h denote the TAS linecuts of representative 3-AMPY-based 2D/3D heterostructures taken at specific delay times to reflect the time taken by the charge carriers to fully populate the ground states of different n-value phases and display the maximum photobleaching before funneling to the 3D-MHPs. 3-AMPY (IPA:DMF) samples present three bleach peaks corresponding to $n = 2$ (2.14 eV), $n = 3$ (1.94 eV) and 3D-MHP at 1.56 eV, consistent with the band-edges of the respective species.[31] A relatively low intensity bleach peak of $n = 2$ and dominant $n = 3$ peak indicates that the $n = 3$ (3-AMPY)$MA_2Pb_3I_{10}$ phase is formed in the majority. The 3-AMPY (TFE:DMF) samples exhibit bleach peaks corresponding

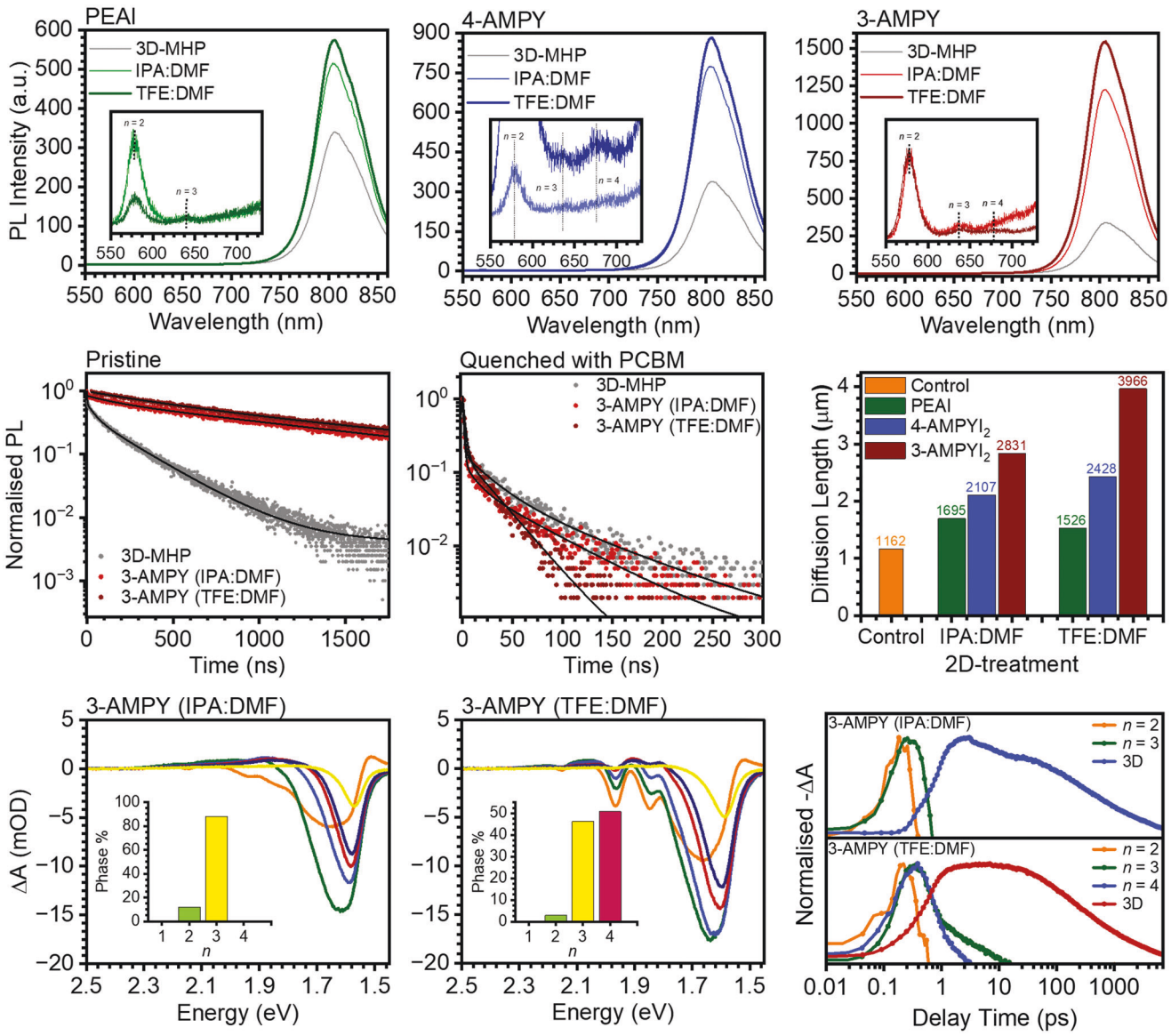

Figure 6. Static PL spectra of 2D/3D heterostructure films comparing 3D-MHP, IPA:DMF- and TFE:DMF-treated films with a) PEAI, b) 4-AMPY, and c) 3-AMPY in the ligand solution. TRPL spectra comparing carrier lifetime of d) bare 3D-MHP, 3-AMPY (IPA:DMF), and 3-AMPY (TFE:DMF) films, respectively, and e) the same films, with PCBM deposited as an electron quenching layer. f) Comparison between electron diffusion length based on the extent of PL quenching after deposition of PCBM. Transient Absorption Spectra of 2D/3D heterostructures based on g) 3-AMPY (IPA:DMF) and h) 3-AMPY (TFE:DMF). The inset represents the relative quantity of 2D-DJPs present on the film based on the maximum amplitude of bleach peak indicating 2D-DJP presence. i) Comparison between charge cascading kinetics of 3-AMPY (IPA:DMF) and 3-AMPY (TFE:DMF) films.

to $n = 2$, 3, 4 and 3D-MHP, with relatively larger bleaching by $n = 3$ and 4. Using the maximum amplitudes of the ground state bleaching peaks (GSBs), the percentage contribution of each 2D-DJP phase can be estimated as shown in the inset of Figures 6g,h. 3-AMPY (TFE:DMF) treatment has afforded the formation of $n = 3$ and 4 in the majority, contributing to almost 90% of total 2D-DJP content. These results also confirm the formation of films dominated by $n = 3$ and 4 during in situ and ex situ GIWAXS of TFE:DMF samples and further explain the trends observed in the PL study. While IPA:DMF does indeed considerably extend the electron diffusion length due to defect passivation, the large density of $n = 2$ phase present can pose an impediment to charge tunneling due to the large quantum-confinement of small-n. In contrast, the TFE:DMF treatment appears to generate DJPs concentrated around $n = 3$ and 4, which should serve as a suitable sweet spot for balancing the enhanced stability of 2D-DJPs while sufficiently low electron tunneling barrier. We observed similar phase distribution dominated by $n = 3$ and 4 in the TAS kinetics of 4-AMPY (TFE:DMF) as noted in Figure S20 (Supporting Information), confirming that TFE is a promising post-processing solvent toward fabricating efficient solar cells capable of generating fewer defects.

Charge carrier dynamics were then elucidated to exemplify the charge build-up and decay (Figure 6i). In 3-AMPY (IPA:DMF),

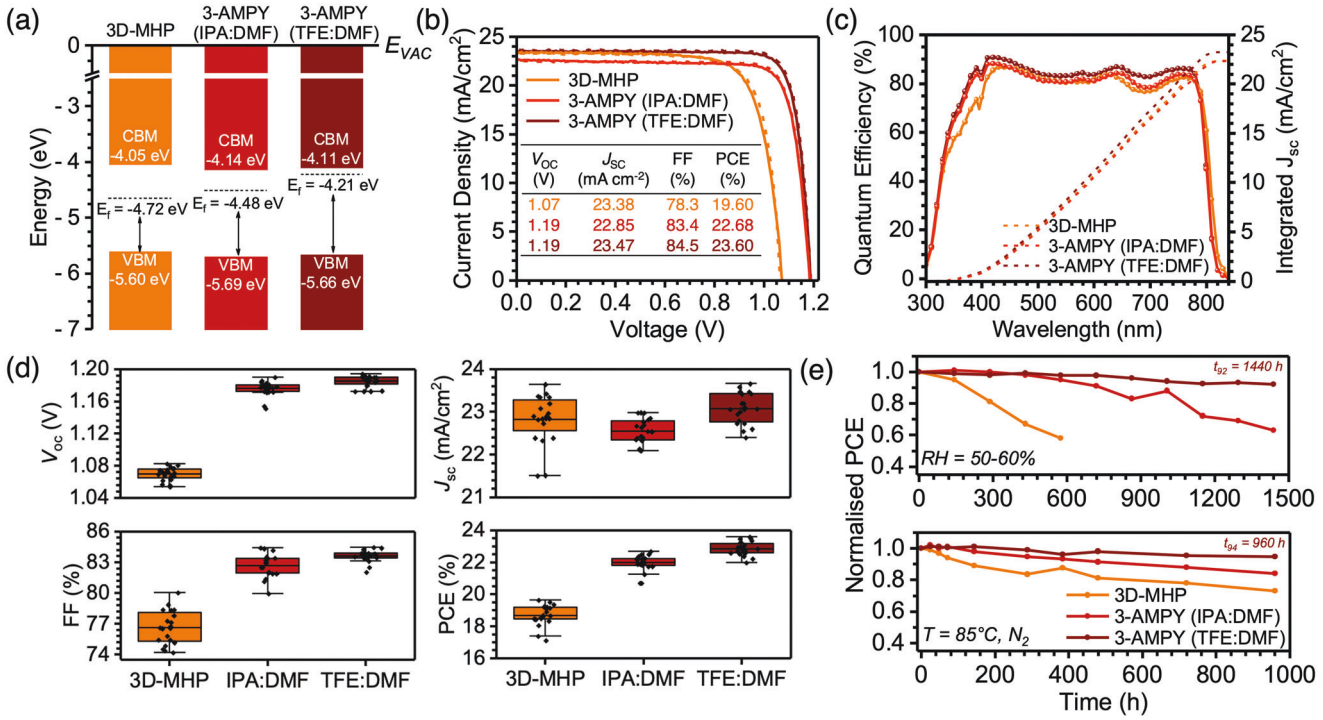

Figure 7. a) Energy level diagram of pristine 3D-MHP and 3-AMPY DJP heterostructures. Device performance of PSCs containing pristine 3D-MHP and 3-AMPY (IPA:DMF) and 3-AMPY (TFE:DMF) heterostructures: b) forward (solid) and reverse (dotted) current density–voltage curves (*J*–*V*), c) external quantum efficiency (EQE) and integrated short-circuit current density, d) statistics of photovoltaic characteristics of reverse scans of PSCs, and e) stability of best-performing PSCs under ambient conditions (RH = 50–60%) (top) and under persistent thermal stress at 85 °C (bottom).

the charge accumulation occurs within 0.1 ps for $n = 2$ and 3, followed by photobleaching decay at 0.3 and 1 ps, respectively. The rapid decay of the 2D-DJPs indicates rapid charge transfer between 2D-DJPs. Subsequently, the 1.56 eV peak of 3D-MHP gradually builds up reaching a maximum at 2 ps before decaying over 7 ns. While the rapid bleaching of the $n = 2$ phase suggests that there is no apparent charge accumulation in the $n = 2$ phase, the delay in the build-up of the 3D-MHP implies a slower 2D-to-3D charge transfer. Like 3-AMPY (IPA:DMF), 3-AMPY (TFE:DMF) sample exhibit a rapid build-up of charge carriers occurring within 0.1 ps for $n = 2$ and 0.2 ps for $n = 3$ and 4 followed by decay over 1, and 10 ps, respectively. The rise of the 3D-MHP occurs at 0.1 ps, eventually reaching a maximum in <2 ps before decaying over 7 ns.

The decay kinetics are extracted by curve fitting the amplitude of the 3D-MHP GSB to multi-exponential functions as listed below:

$$\Delta A = \mathbf{a}_1 e^{\frac{-t}{\tau_1}} + \mathbf{a}_2 e^{\frac{-t}{\tau_2}} + \mathbf{a}_3 e^{\frac{-t}{\tau_3}} - \mathbf{c}_1 e^{\frac{-t}{\tau_{et}}}, \quad (2)$$

where the amplitude is expressed as a convolution of a first-order decay lifetime (τ_1) and energy transfer across phases (τ_{et}) and two slow decay components, ascribed to bimolecular (τ_2) and excitonic trap recombination (τ_3).[54] We have discussed the trends of the fast decay components in this work. We found the energy transfer time constant τ_{et} to be 5.08 and 0.48 ps for 3-AMPY (IPA:DMF) and 3-AMPY (TFE:DMF), respectively. The shorter τ_{et} and rapid rise of the 3D peak can be attributed to the efficient interphase transfer process; the presence of larger n fragments with reduced quantum confinement may lead to efficient charge dissociation at the 2D/3D interface. Furthermore, the bleaching peak of the 3D-components reveals a first-order decay time of 138 and 146 ps, respectively, also suggesting a lower density of traps in line with the PL results.

2.5. Energy Landscape and Photovoltaic Efficiency

Modulating the n distribution across the 2D/3D heterostructure, the defects formed during solvent-induced surface reconstruction and cation choice should collectively influence the energy landscape of the 2D/3D heterostructure toward reducing electron blocking at the film/ETL interface. To examine these effects, we performed surface-sensitive UPS on the 2D/3D films to measure the VBM and fermi-level (E_f) from the top few nm of the films. We performed the energy level calculations based on the fermi level of silver reference (Figure S21a, Supporting Information), optical bandgap (Figure S21b, Supporting Information) and cut-offs extracted from Figure S22a–f (Supporting Information) and summarized in Table S4 (Supporting Information). UPS spectra of the 3D-MHP revealed a typical band structure for a triple-cation 3D-MHP with a VBM at −5.60 eV and E_f of −4.72 eV, implying a slightly more n-type behavior which is typical for Pb-based perovskites (**Figure 7**a). 2D/3D heterostructures with PEAI as cation led to significant downshifting of the VBM and E_f to −5.86 and −4.91 eV, respectively,

attributed to the stronger quantum confinement effect prevalent in 2D-RPPs (Figure S23a, Supporting Information). Similar passivation methods have a comparable downshift in VBM when PEAI was used as a passivator (c.a. 0.2 eV).[17,18] This trend is also consistent with the observed UPS spectra of the $n = 3$ 2D-MHP films in Figure 1c. On the other hand, 3-AMPY (Figure 6a) and 4-AMPY (Figure S23a, Supporting Information) ligands result in shallower VBM because of the shorter interlayer spacing between adjacent inorganic frameworks affording stronger I–I antibonding interactions.[34] 3-AMPY benefitted from the smallest interlayer spacing of 3.6 Å and possessed the smallest VBM offsets of c.a. 0.06–0.09 eV with respect to the 3D-MHP.

Interestingly, we found very little difference in VBM position upon varying solvent for a selected ligand (Figure 7a; Figure S23b, Supporting Information). However, there is a profound influence on the E_f and CBM location with increasing n. We observed strikingly shallower E_fs for DJP-based 2D/3D heterostructures fabricated via TFE:DMF solvent compared to their 3D-MHP counterparts irrespective of ligand (Figure S23a, Supporting Information). The E_f of 2D-MHPs also tends to shift toward increasingly n-type behavior with decreasing quantum-confinement. IPA:DMF treated films possess large trap density, as evidenced by TRPL even after passivation. Leaching of small cations from the perovskite surface causes local FA^+/MA^+ deficiencies resulting in a more p-type nature (IPA:DMF), while one rich in organic cations exhibits n-type behavior (e.g., TFE:DMF). Most notably, 3-AMPY (TFE:DMF) leverages the formation of large n and low defect density to yield a E_f of −4.21 eV, creating favorable band bending with the CBM of the 3D-MHP for electron extraction (Figure 7a).

Motivated by the favorable energy landscape and charge carrier dynamics, we examined the impact of the new solvent treatment of forming 2D/3D heterostructures on the solar cell characteristics of a typical p–i–n stack: ITO | 2PACz | Perovskite | PCBM | C_{60} | BCP | Ag with different surface treatments (PEAI, 4-AMPY, and 3-AMPY in IPA:DMF or TFE:DMF, Figure S24, Supporting Information). In agreement with our findings that reducing the quantum confinement via rational ligand selection leads to more efficient carrier extraction and electron tunneling, 3-AMPY-based 2D/3D heterostructures unanimously outperform the 4-AMPY and PEAI-treated devices. The elimination of the Van der Waals gap in the DJP capping layers has afforded improvements in FF compared to the RPP capping layer from PEAI, while the fine-tuned band alignment of 3-AMPY devices results in a reduced electron tunneling barrier with dramatic improvements in V_{oc} up to 1.19 V (Figure 7b). Moreover, in agreement with our findings that TFE:DMF treatment results in a uniformly mixed 2D-DJP capping layer dominated by $n \geq 3$ phases that enables long electron diffusion lengths, the 3-AMPY (TFE:DMF) devices have outperformed the 3-AMPY (IPA:DMF), as shown in Figure 7b. The improved performance of the TFE:DMF solar cells compared to the IPA:DMF counterparts arises from a slight increase in FF and J_{sc} (83.4% to 84.5% and 22.85 to 23.47 mA cm^{-2} for 3-AMPY, respectively). As a result, a champion device efficiency of 23.60% was obtained. The J_{SC} of 23.47 mA cm^{-2} is also within a 5% mismatch of the integrated current density from the EQE spectra (23.1 mA cm^{-2}) in Figure 7c. Further analyzing the EQE spectrum of the champion device via the first derivative reveals a bandgap of 1.55 eV, recording a voltage loss (V_{oc}^{loss}) of 0.36 V (Figure S25, Supporting Information). The improvements in these solar cell figure of merits validate the translatability of the observed enhancements in carrier dynamics, elongated electron diffusion and interfacial band alignment that stem from tailoring 2D-DJP phase distribution atop the 3D-MHP via an inert 2D-DJP processing solvent. The combined enhancement of the photovoltaic characteristics was verified statistically through a comparison of 20 individual devices, with an average PCE of 18.71% ± 0.65% for the 3D-MHP, 21.92% ± 0.53% for the 3-AMPY (IPA:DMF) and 22.98% ± 0.35% for the 3-AMPY (TFE:DMF), respectively (Figure 7d).

Finally, we investigated the long-term stability of the devices to verify the resilience of the 2D/3D heterostructures toward ambient and thermal stress. In practice, 2D/3D perovskites have been shown to display a drop in PCE under persistent thermal stress over a few hours.[55] Thus, it is critical to ascertain the ambient and thermal stability (Note S6 and Figure S26, Supporting Information) of the new ligands used in our study. We subjected solar cells of 3-AMPY and PEAI heterostructures from the representative solvents used in this study and periodically monitored their PCEs under the influence of relative humidity (RH = 50–60%, Figure 7e top panel; Figure S26, Supporting Information) and temperature (85 °C, Figure 7e bottom panel; Figure S27, Supporting Information). The 3D-MHP PSCs drop to 58% of their original PCE within 600 h of ambient exposure. However, 2D treatment has significantly prolonged the shelf-life of the PSCs. In particular, the devices fabricated via TFE:DMF solvent have retained 90% and 92% of their original PCEs after 1500 h with PEAI and 3-AMPY as the respective ligands. In stark contrast, the IPA:DMF based films degrade rapidly to c.a. 65% after a similar timeframe, confirming our hypothesis that exposing the $[PbI_6]^{4-}$ framework of the 3D-MHP during post-treatment using surface destructive solvent (IPA:DMF) is a suboptimal passivation method that generates surface defects.

More critically, the 2D-treated films also exhibit curious trends during thermal stress tests. Particularly, the PEAI-based 2D/3D devices are characterized by an initial rapid fall in PCE to c.a. 73% of their original values, followed by a period of relative stability up to 384 h. The PEAI (TFE:DMF) devices eventually drop to 47% of their original PCEs in 1000 h, with overall lower device stability compared to the 3D-MHP counterparts (Figure S28, Supporting Information). 3-AMPY (TFE:DMF) on the other hand exhibits a t_{92} of 960 h, while 3-AMPY (IPA:DMF) retains 83% of its original PCE, proving that mitigating surface reconstruction is a more efficient route to fabricating 2D/3D heterostructures. Thus, we are able to leverage the rigid lattice and superior charge transport of 2D-DJPs as capping layers without sacrificing the structural integrity of the underlying 3D-MHPs to fabricate efficient and stable solar cells.

3. Conclusion

In summary, we compared the solvent-mediated formation dynamics of 2D-on-3D perovskites and translated the insights to tailor the energy landscape, enabling efficient and stable inverted perovskite solar cells via synergistic ligand engineering. Fabricating 2D/3D heterostructures with IPA as a processing solvent leads to diffusion-limited formation of a graded

2D-capping layer with smaller *n* initially at the top 2D-MHP surface, and larger *n* later, buried closer to the 2D/3D heterostructure interface. In contrast, TFE allows crystallization of larger *n* first and smaller *n* very shortly after, forming uniformly distributed domains along the cross section of the 2D-MHP layer. Additionally, using DJP-forming ligands 3-AMPY and 4-AMPY in conjunction with TFE enabled formation of 2D-capping layers dominated by $n = 3$ and 4. The preponderance of large *n* DJPs in the capping layer significantly reduced defect density, elongated electron diffusion length and created favorable band bending to facilitate efficient electron tunneling. As a result, inverted 2D/3D PSCs based on 3-AMPY and TFE-based solvent leverage these advantages to deliver a champion power conversion efficiency of 23.60% with a remarkable V_{oc} and FF of 1.19 V and 84.5%, respectively, with high stability toward moisture ingress and thermal stress. Taken together, the interplay between surface states before passivation, emergent formation dynamics of 2D/3D heterostructures and band energy modulation with DJPs will further guide the experimental and theoretical design of efficient and stable p–i–n solar cells through surface engineering.

Supporting Information

Supporting Information is available from the Wiley Online Library or from the author.

Acknowledgements

This work was financially supported by the NSF ECCS-2054942 and EPM-2114350. This work made use of the Cornell Center for Materials Research Shared Facilities which are supported through the NSF MRSEC program (DMR-1719875) and the GIWAXS and TAS from the resources of the Centre for Functional Nanomaterials and the CMS beamline (11-BM) of the National Synchrotron Light Source II, both supported by the U.S. DOE Office of Science Facilities at Brookhaven National Laboratory under Contract No. DE-SC0012704.

Conflict of Interest

The authors declare no conflict of interest.

Data Availability Statement

The data that support the findings of this study are available from the corresponding author upon reasonable request.

Keywords

2D/3D heterostructures, Dion–Jacobson perovskite, inverted solar cells, in situ X-ray scattering, surface reconstruction

Received: July 13, 2023
Revised: September 4, 2023
Published online:

[1] X. Li, J. M. Hoffman, M. G. Kanatzidis, *Chem. Rev.* **2021**, *121*, 2230.
[2] P. Liu, N. Han, W. Wang, R. Ran, W. Zhou, Z. Shao, *Adv. Mater.* **2021**, *33*, 2002582.
[3] B. Saparov, D. B. Mitzi, *Chem. Rev.* **2016**, *116*, 4558.
[4] Y. Gao, E. Shi, S. Deng, S. B. Shiring, J. M. Snaider, C. Liang, B. Yuan, R. Song, S. M. Janke, A. Liebman-Peláez, P. Yoo, M. Zeller, B. W. Boudouris, P. Liao, C. Zhu, V. Blum, Y. Yu, B. M. Savoie, L. Huang, L. Dou, *Nat. Chem.* **2019**, *11*, 1151.
[5] L. Mao, C. C. Stoumpos, M. G. Kanatzidis, *J. Am. Chem. Soc.* **2019**, *141*, 1171.
[6] Z. Xu, D. Lu, X. Dong, M. Chen, Q. Fu, Y. Liu, *Adv. Mater.* **2021**, *33*, 2105083.
[7] S. Sidhik, Y. Wang, W. Li, H. Zhang, X. Zhong, A. Agrawal, I. Hadar, I. Spanopoulos, A. Mishra, B. Traoré, M. H. K. Samani, C. Katan, A. B. Marciel, J. C. Blancon, J. Even, A. Kahn, M. G. Kanatzidis, A. D. Mohite, *Cell Rep. Phys. Sci.* **2021**, *2*, 100601.
[8] M. Shao, T. Bie, L. Yang, Y. Gao, X. Jin, F. He, N. Zheng, Y. Yu, X. Zhang, *Adv. Mater.* **2022**, *34*, 2107211.
[9] Z. Li, B. Li, X. Wu, S. A. Sheppard, S. Zhang, D. Gao, N. J. Long, Z. Zhu, *Science* **2022**, *376*, 416.
[10] H. J. Mun, M. G. Kim, T. J. Shin, S. Il Seok, *Nature* **2023**, *616*, 724.
[11] T. Yang, L. Gao, J. Lu, C. Ma, Y. Du, P. Wang, Z. Ding, S. Wang, P. Xu, D. Liu, H. Li, X. Chang, J. Fang, W. Tian, Y. Yang, *Nat. Energy* **2023**, *14*, 839.
[12] M. A. Mahmud, T. Duong, J. Peng, Y. Wu, H. Shen, D. Walter, H. T. Nguyen, N. Mozaffari, G. D. Tabi, K. R. Catchpole, K. J. Weber, T. P. White, *Adv. Funct. Mater.* **2022**, *32*, 2009164.
[13] J. W. Lee, S. Tan, S. Il Seok, Y. Yang, N. G. Park, *Science* **2022**, *375*, eabj1186.
[14] A. A. Sutanto, P. Caprioglio, N. Drigo, Y. J. Hofstetter, I. Garcia-Benito, V. I. E. Queloz, D. Neher, M. K. Nazeeruddin, M. Stolterfoht, Y. Vaynzof, G. Grancini, *Chem* **2021**, *7*, 1903.
[15] G. Wu, R. Liang, M. Ge, G. Sun, Y. Zhang, G. Xing, *Adv. Mater.* **2022**, *34*, 2105635.
[16] X. Lin, D. Cui, X. Luo, C. Zhang, Q. Han, Y. Wang, L. Han, *Energy Environ. Sci.* **2020**, *13*, 3823.
[17] S. Gharibzadeh, P. Fassl, I. M. Hossain, P. Rohrbeck, M. Frericks, M. Schmidt, T. Duong, M. R. Khan, T. Abzieher, B. A. Nejand, F. Schackmar, O. Almora, T. Feeney, R. Singh, D. Fuchs, U. Lemmer, J. P. Hofmann, S. A. L. Weber, U. W. Paetzold, *Energy Environ. Sci.* **2021**, *14*, 5875.
[18] Y. Huang, K. Yan, B. Niu, Z. Chen, E. Gu, H. Liu, B. Yan, J. Yao, H. Zhu, H. Chen, C.-Z. Li, *Energy Environ. Sci.* **2023**, *16*, 557.
[19] M.-G. La-Placa, L. Gil-Escrig, D. Guo, F. Palazon, T. J. Savenije, M. Sessolo, H. J. Bolink, *ACS Energy Lett.* **2019**, *4*, 2893.
[20] S. Sidhik, Y. Wang, M. De Siena, R. Asadpour, A. J. Torma, T. Terlier, K. Ho, W. Li, A. B. Puthirath, X. Shuai, A. Agrawal, B. Traore, M. Jones, R. Giridharagopal, P. M. Ajayan, J. Strzalka, D. S. Ginger, C. Katan, M. A. Alam, J. Even, M. G. Kanatzidis, A. D. Mohite, *Science* **2022**, *377*, 1425.
[21] X. Zhong, X. Ni, S. Sidhik, H. Li, A. D. Mohite, J. L. Brédas, A. Kahn, *Adv. Energy Mater.* **2022**, *12*, 2202333.
[22] T. Kodalle, R. F. Moral, L. Scalon, R. Szostak, M. Abdelsamie, P. E. Marchezi, A. F. Nogueira, C. M. Sutter-Fella, *Adv. Energy Mater.* **2022**, *13*, 2201490.
[23] M. He, J. Liang, Z. Zhang, Y. Qiu, Z. Deng, H. Xu, J. Wang, Y. Yang, Z. Chen, C.-C. Chen, *J. Mater. Chem. A* **2020**, *8*, 25831.
[24] Y. Du, Q. Tian, S. Wang, T. Yang, L. Yin, H. Zhang, W. Cai, Y. Wu, W. Huang, L. Zhang, K. Zhao, S. (.F.). Liu, *Adv. Mater.* **2022**, *35*, 2206451.
[25] K. Ma, J. Sun, H. R. Atapattu, B. W. Larson, H. Yang, D. Sun, K. Chen, K. Wang, Y. Lee, Y. Tang, A. Bhoopalam, L. Huang, K. R. Graham, J. Mei, L. Dou, *Sci. Adv.* **2023**, *9*, eadg0032.
[26] D. Chen, L. Wang, X. Luo, H. Xie, X. Chen, *Nat. Photonics* **2022**, *16*, 358.

[27] S. Tan, T. Huang, I. Yavuz, R. Wang, M. H. Weber, Y. Zhao, M. Abdelsamie, M. E. Liao, H.-C. Wang, K. Huynh, K.-H. Wei, J. Xue, F. Babbe, M. S. Goorsky, J.-W. Lee, C. M. Sutter-Fella, Y. Yang, *J. Am. Chem. Soc.* **2021**, *143*, 6781.
[28] S. Tan, I. Yavuz, M. H. Weber, T. Huang, C.-H. Chen, R. Wang, H.-C. Wang, J. H. Ko, S. Nuryyeva, J. Xue, Y. Zhao, K.-H. Wei, J.-W. Lee, Y. Yang, *Joule* **2020**, *4*, 2426.
[29] X. Xiao, M. Wu, Z. Ni, S. Xu, S. Chen, J. Hu, P. N. Rudd, W. You, J. Huang, *Adv. Mater.* **2020**, *32*, 2004080.
[30] C. C. Stoumpos, D. H. Cao, D. J. Clark, J. Young, J. M. Rondinelli, J. I. Jang, J. T. Hupp, M. G. Kanatzidis, *Chem. Mater.* **2016**, *28*, 2852.
[31] X. Li, W. Ke, B. Traoré, P. Guo, I. Hadar, M. Kepenekian, J. Even, C. Katan, C. C. Stoumpos, R. D. Schaller, M. G. Kanatzidis, *J. Am. Chem. Soc.* **2019**, *141*, 12880.
[32] Z. Shi, Z. Ni, J. Huang, *ACS Energy Lett.* **2022**, *7*, 984.
[33] X. Li, W. Ke, B. Traoré, P. Guo, I. Hadar, M. Kepenekian, J. Even, C. Katan, C. C. Stoumpos, R. D. Schaller, M. G. Kanatzidis, *J. Am. Chem. Soc.* **2019**, *141*, 12880.
[34] R. Prasanna, A. Gold-Parker, T. Leijtens, B. Conings, A. Babayigit, H.-G. Boyen, M. F. Toney, M. D. Mcgehee, *J. Am. Chem. Soc.* **2017**, *139*, 11117.
[35] Y. Fu, T. Wu, J. Wang, J. Zhai, M. J. Shearer, Y. Zhao, R. J. Hamers, E. Kan, K. Deng, X.-Y. Zhu, S. Jin, *Nano Lett.* **2017**, *17*, 4405.
[36] R. Azmi, E. Ugur, A. Seitkhan, F. Aljamaan, A. S. Subbiah, J. Liu, G. T. Harrison, M. I. Nugraha, M. K. Eswaran, M. Babics, Y. Chen, F. Xu, T. G. Allen, A. Rehman, C. Wang, T. D. Anthopoulos, U. Schwingenschlögl, M. De Bastiani, E. Aydin, S. De Wolf, *Science* **2022**, *5784*, 73.
[37] J. J. Yoo, S. Wieghold, M. C. Sponseller, M. R. Chua, S. N. Bertram, N. T. P. Hartono, J. S. Tresback, E. C. Hansen, J.-P. Correa-Baena, V. Bulovic, T. Buonassisi, S. S. Shin, M. G. Bawendi, *Energy Environ. Sci.* **2019**, *12*, 2192.
[38] A. H. Proppe, A. Johnston, S. Teale, A. Mahata, R. Quintero-Bermudez, E. H. Jung, L. Grater, T. Cui, T. Filleter, C.-Y. Kim, S. O. Kelley, F. De Angelis, E. H. Sargent, *Nat. Commun.* **2021**, *12*, 3472.
[39] D. Zhang, H. Zhang, H. Guo, F. Ye, S. Liu, Y. Wu, *Adv. Funct. Mater.* **2022**, *32*, 2200174.
[40] J. Hou, W. Li, H. Zhang, S. Sidhik, J.-C. Blancon, J. Even, M. G. Kanatzidis, A. D. Mohite, https://doi.org/10.48550/arXiv.2212.00989 **2022**.
[41] M. Avrami, *J. Chem. Phys.* **1939**, *7*, 1103.
[42] M. Avrami, *J. Chem. Phys.* **1940**, *8*, 212.
[43] M. Avrami, *J. Chem. Phys.* **1941**, *9*, 177.
[44] J. Dong, S. Shao, S. Kahmann, A. J. Rommens, D. Hermida-Merino, G. H. ten Brink, M. A. Loi, G. Portale, *Adv. Funct. Mater.* **2020**, *30*, 2070154.
[45] Y. Fu, W. Zheng, X. Wang, M. P. Hautzinger, D. Pan, L. Dang, J. C. Wright, A. Pan, S. Jin, *J. Am. Chem. Soc.* **2018**, *140*, 15675.
[46] J. Xi, J. Jiang, H. Duim, L. Chen, J. You, G. Portale, S. (.F.). Liu, S. Tao, M. A. Loi, *Adv. Mater.* **2023**, *35*, 2302896.
[47] A. Jana, Q. Ba, A. S. Nissimagoudar, K. S. Kim, *J. Mater. Chem. A* **2019**, *7*, 25785.
[48] F. Ji, L. Wang, S. Pang, P. Gao, H. Xu, G. Xie, J. Zhang, G. Cui, *J. Mater. Chem. A* **2016**, *4*, 14437.
[49] C. Zhang, S. Wu, L. Tao, G. M. Arumugam, C. Liu, Z. Wang, S. Zhu, Y. Yang, J. Lin, X. Liu, R. E. I. Schropp, Y. Mai, *Adv. Energy Mater.* **2020**, *10*, 2002004.
[50] T. He, S. Li, Y. Jiang, C. Qin, M. Cui, L. Qiao, H. Xu, J. Yang, R. Long, H. Wang, M. Yuan, *Nat. Commun.* **2020**, *11*, 1672.
[51] M. Kaiser, Y. Li, I. Allegro, B. S. Richards, U. W. Paetzold, I. A. Howard, *Adv. Mater. Interfaces* **2021**, *8*, 2101326.
[52] S. Shao, H. Duim, Q. Wang, B. Xu, J. Dong, S. Adjokatse, G. R. Blake, L. Protesescu, G. Portale, J. Hou, M. Saba, M. A. Loi, *ACS Energy Lett.* **2020**, *5*, 39.
[53] M. J. P. Alcocer, T. Leijtens, L. M. Herz, A. Petrozza, H. J. Snaith, *Science* **2013**, *342*, 341.
[54] J. Liu, J. Leng, K. Wu, J. Zhang, S. Jin, *J. Am. Chem. Soc.* **2017**, *139*, 1432.
[55] A. A. Sutanto, R. Szostak, N. Drigo, V. I. E. Queloz, P. E. Marchezi, J. C. Germino, H. C. N. Tolentino, M. K. Nazeeruddin, A. F. Nogueira, G. Grancini, *Nano Lett.* **2020**, *20*, 3992.